CONF-9109256--2

DE92 011787

To be published in Proceedings of the 10th Pfefferkorn Conference on Signal and Image Processing, Cambridge, United Kingdom, September 16–19, 1991

SUB-ÅNGSTROM MICROSCOPY THROUGH INCOHERENT IMAGING AND IMAGE RECONSTRUCTION

S. J. Pennycook, D. E. Jesson, and M. F. Chisholm
Solid State Division, Oak Ridge National Laboratory
Oak Ridge, Tennessee 37831-6030, U.S.A.

and

A. G. Ferridge and M. J. Seddon
The Wellcome Research Laboratories
Beckenham, Kent BR33BS United Kingdom

SOLID STATE DIVISION
OAK RIDGE NATIONAL LABORATORY
Managed by
MARTIN MARIETTA ENERGY SYSTEMS, INC.
under
Contract No. DE-AC05-84OR21400
with the
U.S. DEPARTMENT OF ENERGY
Oak Ridge, Tennessee 37831-6030

March 1992

SUB-ÅNGSTROM MICROSCOPY THROUGH INCOHERENT IMAGING AND IMAGE RECONSTRUCTION

S. J. Pennycook, D. E. Jesson, and M. F. Chisholm
Solid State Division, Oak Ridge National Laboratory
Oak Ridge, Tennessee 37831-6030, U.S.A.
and
A. G. Ferridge and M. J. Seddon
The Wellcome Research Laboratories
Beckenham, Kent BR33BS United Kingdom

ABSTRACT

Z-contrast scanning transmission electron microscopy (STEM) with a high-angle annular detector breaks the coherence of the imaging process, and provides an incoherent image of a crystal projection. Even in the presence of strong dynamical diffraction, the image can be accurately described as a convolution between an object function, sharply peaked at the projected atomic sites, and the probe intensity profile. Such an image can be inverted intuitively without the need for model structures, and therefore provides the important capability to reveal unanticipated interfacial arrangements. It represents a *direct* image of the crystal projection, revealing the location of the atomic columns and their relative high-angle scattering power. Since no phase is associated with a peak in the object function or the contrast transfer function, extension to higher resolution is also straightforward. Image restoration techniques such as maximum entropy, in conjunction with the 1.3 Å probe anticipated for a 300 kV STEM, appear to provide a simple and robust route to the achievement of sub-Ångstrom resolution electron microscopy.

Introduction

A scan through these proceedings will reveal a large number of different approaches to the determination of crystal structures at resolutions approaching or beyond 1 Å. All these techniques however are based on coherent imaging or diffraction and have major problems associated either with the inversion of the data (the phase problem), or, if the sample has any significant thickness, with non-linear imaging, so that images can then be used only to choose between a small number of likely model structures.

Incoherent imaging, as realized in the Z-contrast technique, offers a new approach to high resolution structure determination. Though it may be felt that destroying the phase information must inevitably result in a loss of information, in practice, this is more than compensated for by the enormous resultant gain in image interpretability. We never attempt to recover the wave function at the crystal exit face, nor the projected crystal potential, and therefore we effectively bypass the phase problem of electron diffraction and the limitations of non-linear imaging mentioned above.

Z-contrast electron microscopy provides linear incoherent imaging of an *object function*, in which the effects of dynamical diffraction are included, although they appear only as a second order correction to the high-angle scattering power. The object function is highly local, making supercell calculations obsolete, and sharply peaked at the projected atomic columns, so that resolution enhancement by a factor of two becomes a straightforward proposition. Below we describe briefly how these important characteristics arise and demonstrate the potential for maximum entropy image enhancement to extract direct structural information on the sub-Ångstrom scale.

Breaking the Coherence of the Imaging Process.

Incoherent imaging theory can be used whenever a large number of routes of comparable amplitude but uncorrelated phases contribute to the image intensity. In our case the image intensity for a given probe position is the integrated intensity reaching the high-angle annular detector, and effective three dimensional incoherence can be established by ensuring that the detector collects predominantly multiphonon thermal diffuse scattering events. The high-angle detector was first proposed by Howie in 1978, and since it plays a critical role in establishing incoherent imaging at atomic resolutions, we shall refer to it as the Howie detector.

Consider a crystal in a zone axis orientation with the scattering geometry shown in Fig 1. The detector geometry itself can average sufficient fringes in the transverse plane to ensure that atomic columns are imaged with improved resolution and without contrast reversals, even if coherent scattering dominates the detected signal (Jesson and Pennycook 1990 and in press). However, the shape factor surrounding each reciprocal lattice spot in the beam direction ensures that for crystals of thickness $t >> 2\lambda/\theta^2$ (where λ is the electron wavelength and θ the scattering angle) there is substantial destructive interference from atoms at different depths, and very little amplitude results from the column as a whole (i.e., the Ewald sphere cuts only the tails of the shape factors).

Now consider the situation with a vibrating crystal. Hall (1965) has shown that at high scattering angles, multiphonon scattering (the simultaneous emission and/or absorption of several phonons in a single scattering event) is an order of magnitude more probable than single-phonon scattering. Sidebands form at $\pm\,\theta$ about each reciprocal lattice point, where θ is the sum of phonon wavevectors involved in the multiphonon scattering event. Due

to the large number of possible routes to a given θ, a broad, continuous distribution forms in reciprocal space. The Ewald sphere samples all points on the shape factor, effectively integrating over the shape factor to give an intensity proportional to t ; i.e., the intensity detected from the column of atoms is now precisely the intensity that would have been detected if the atoms were acting as incoherent emitters of electrons. Note that this is an effective incoherence in the z direction since there is insufficient z momentum transfer to localize the interaction at a single atom.

The Einstein model of independently vibrating atoms is the ideal model for this situation, and we can construct a 2D projected potential $V^{HA}(\mathbf{R})$ for the diffuse scattering generated incoherently by the unit cell at position **R**. The total intensity reaching the detector I^{HA} will then be given by the total rate of loss from the incident wavefield $\psi(\mathbf{r})$,

$$I^{HA} = \frac{2}{\hbar v} \int |\psi(\mathbf{r})|^2 V^{HA}(\mathbf{R})\, d\mathbf{r} \ , \qquad (1)$$

where $\hbar$ is Planck's constant and v the electron velocity, which is exactly analogous to the calculation of absorption effects in dynamical diffraction (Hall and Hirsch 1965), and the generation of X rays (Cherns, Howie, and Jacobs 1973) or low-energy photons (Pennycook and Howie (1980)). Explicit expressions for $V^{HA}(\mathbf{R})$ can be obtained following the treatment of Hall and Hirsch.

To ensure that the detected signal is dominated by diffuse scattering generally requires inner detector angles of 75 mrad or so, in which case the relevant potential for high-angle scattering is very sharply peaked at the projected atom sites, with a width of the order of 0.2 Å, much sharper than the

variations in $\psi(r)$. It is often convenient therefore to make a sharp potential approximation, replacing Eq. (1) by

$$I^{HA} = \frac{2}{\hbar v} \sum_{\kappa} |\psi(r_\kappa)|^2 \int V^{HA}(R)dR = \sum_{\kappa} |\psi(r_k)|^2 \sigma_\kappa \,. \qquad (2)$$

The electron intensity is assumed constant over the spatial extent of each atomic high-angle potential which may therefore be integrated directly into the diffuse scattering cross section σ_κ, given by

$$\sigma_\kappa = \left(\frac{4\pi\gamma}{\chi}\right)^2 \int_{\text{detector}} f_\kappa^2(s) \left[1 - e^{-2M_\kappa s^2}\right] d^2s \qquad (3)$$

where γ is the relativistic mass correction factor, χ the wave vector, f the full atomic scattering factor, $s = \theta/2\lambda$, and $M = 8\pi^2\bar{u}^2$ where $\bar{u}^2$ is the mean square thermal vibration amplitude.

In this approximation of complete localization of the interaction, the high-angle form of the diffuse scattering is identical to that for isolated atoms, and the total intensity scattered by each atom is proportional to the incident electron intensity at its site; the detector has been effectively transferred to the atom sites themselves.

The situation for a phase object is shown schematically in Fig. 2. The electron intensity inside the crystal is, by definition, just the incident probe intensity profile $P^2(R)$, and Eq (1) represents the simple convolution

$$I^{HA}(R) = O(R) * P^2(R). \qquad (4)$$

where

$$O(R) = \frac{2}{\hbar v} V^{HA}(R), \tag{5}$$

is the object function for the crystal. In the limit of complete localization, this can be written as

$$O(R) = \sum_{\kappa} \sigma_{\kappa} \delta(R - R_i) \tag{6}$$

Reducing Dynamical Effects to Second Order

By breaking the coherence of the imaging process, the Howie detector makes a Z-contrast image fundamentally different from a phase contrast image. The Z-contrast image does not depend on the phase of the electron wave function emerging at the exit face of the sample; it depends on the integrated intensity at all atom sites in the sample . Phase contrast imaging uses the low order Fourier components of *all* Bloch states (the diffracted beam amplitudes), which leads to strong interference effects as a function of thickness and strong proximity effects at interfaces. Z-contrast imaging uses *only* those Bloch states that contribute to the intensity at the atom sites, tightly bound s-type Bloch states, and their high-order Fourier components *all* contribute to the total intensity at the atom sites.

As an illustration consider the case of a Si_2Ge_2 superlattice. Two highly localized Bloch states are shown in Fig. 3, corresponding to bonding *s*-type molecular orbitals located over the Si and Ge dumbbells respectively, and also two less localized states, one centered primarily over the Ge dumbbell, the other representing a hybridization of a Ge 2s state with the 2p states of the weaker Si strings. Only the 1s-type molecular orbital states contribute significantly to the high-angle scattering, firstly because their peaks coincide with the peak in the high-angle potential, and, secondly, because tightly bound states are non-dispersive so that states excited by each incident angle in the

STEM probe add constructively. Less localized states tend to interfere destructively during this angular integration, and in the case of p-type states for example, tend to have minima at the atom sites. It is an excellent approximation to consider the high-angle scattering as being generated entirely by s states with the result that dynamical diffraction effects, the interference of Bloch state components with comparable amplitudes, are reduced to second order (Pennycook and Jesson 1990, 1991). The *Z*-contrast image intensity increases monotonically with thickness, until the s states become absorbed, at which point the image contrast slowly reduces due to the increasing background from all other states.

The image can again be written as a convolution, where the object function including absorption is given in the limit of complete localization by

$$O(R,t) = \sum_i \sigma_i \varepsilon^{1s^2}(0)\tau^{1s^2}(R,0)\left(\frac{1-e^{-2\mu^{1s}(0)t}}{2\mu^{1s}(0)}\right)\delta(R - R_i) \qquad (7)$$

where $\sigma_i = \frac{1}{t}\sum_\kappa \sigma_\kappa$ is the columnar cross section and and $P^2(R)$ is replaced by

$$P^2_{eff}(R) = \left|\frac{1}{\varepsilon^{1s}(0)}\int_{\substack{\text{objective}\\\text{aperture}}} \varepsilon^{1s}(K)e^{i[K\cdot(R - R_O) + \gamma(K)]}dK\right|^2 \qquad (8)$$

an effective probe intensity profile which includes the small angular fall-off in s state excitation but nevertheless has a width close to that of the incident probe. Comparing with the object function in Eq. 6, it is clear that the columnar high-angle cross sections are scaled by the integrated s state intensity along the column, which can be regarded as the channeling effect of that column. The fact that these channeling effects are relatively insensitive to

column composition is the key reason that images always behave as expected intuitively, that image contrast directly reflects changes in the high-angle cross sections. Ge columns appear brighter than Si columns at all thicknesses, even though the actual intensity ratio will depend on crystal thickness due to differences in s state absorption. It is also possible to write an object function that changes smoothly from the phase object regime to the independent s state regime (Pennycook and Jesson in press).

These object functions are highly local; the tightly bound s states are the states least sensitive to the nature and arrangement of surrounding strings. Furthermore we need only the intensity of the s states not their emergent phase at the crystal exit face. Small overlaps with the tails of the potentials from surrounding strings will have a similar effect to a change in the mean inner potential, and will change the s state eigenvalue (and hence the emergent phase) but not the intensity. Note that in phase contrast imaging, such small changes in the eigenvalue are directly converted to changes in the image intensity (Kambe 1982), so that strong proximity effects would be likely even if only s-states were involved in the imaging. Of course, less localized states are also involved in phase contrast imaging, which are far more sensitive to overlaps with neighboring strings, for example the two lower states in Fig. 2. Therefore proximity effects are inherent in phase contrast imaging and supercell calculations of model interface structures are essential.

For Z-contrast imaging, not only are supercell calculations unnecessary but object functions for complex structures can be assembled column by column using s states calculated from model unit cells. Provided the cell size is sufficient to avoid strong overlaps, the s state intensity will be equal to that of an isolated string. If significant overlap is anticipated, for example the Si and Ge dumbbells in Fig. 2, then appropriate molecular orbital calculations

can also be done using model unit cells. The use of small model unit cells, and the need to calculate only axial Bloch states and the dispersion surface represents a vast saving in computer time compared to full calculations.

Intuitive Image Inversion

With an optimum imaging probe, the highly local object function will be converted into an image which is sufficiently local for image inversion to be intuitive. Of course, if strong tails are present on the probe it will be very difficult to visualize the effects of the convolution and the benefits of the highly local object function will be lost. The optimum conditions were analyzed by Scherzer (1949) and Crewe and coworkers Salzman (1982), who arrived at the conditions

$$\alpha_{opt} = \left(\frac{4\lambda}{C_s}\right)^{1/4} \tag{9}$$

$$\Delta f_{opt} = -(C_s\lambda)^{1/2} \tag{10}$$

where α is the objective aperture semiangle, C_s the objective lens spherical aberration coefficient, and Δf the defocus. This results in a probe intensity profile very similar to an Airy disc in light optics, so that the resolution limit can be defined using a simple two point Rayleigh criterion, as

$$d_{min} = \frac{0.61\,1}{\alpha_{opt}} = 0.43\,C_s^{1/4}\lambda^{3/4} \tag{11}$$

which is very close to the radius of the first intensity minimum and to the FWHM of the central peak. Note that we do see the substantial improvement in resolution expected from incoherent imaging. Note also that the optimum imaging probe does not depend on the spacings we anticipate in the object. Direct imaging of interface structure and composition can now be achieved

with no pretuning of the microscope conditions and no need for any preconceived ideas concerning likely model structures. Unanticipated effects will be immediately apparent and can give dramatic insight into interfacial properties and materials growth mechanisms.

Consider for example the possibility for column-by-column compositional mapping in the $Si_{1-x}Ge_x$ system. The s-state molecular orbital intensity varies little with alloy composition x, as shown in Fig. 4. This is because with increasing string strength, although the state becomes more sharply peaked at the atomic sites, its excitation becomes correspondingly reduced. As a function of thickness, the ratio of Ge to Si s-state intensities show a general decrease, reflecting the higher absorption of the Ge column (Fig. 5). The full dynamical calculation indicates a dynamical enhancement for Ge at small thicknesses of about 20% over the s-state prediction, although this is second order compared to the cross section ratio of 3.7. Thus columns seen brighter necessarily contain more Ge, and the image can be approximately inverted intuitively. Unexpected interfacial arrangements will be immediately seen from the form of the image, though for accurate compositional mapping the thickness should be known so that the dynamical factors can be accounted for.

Of course, we can only invert the *projected* structure, since the elemental distribution along a column has only a second order effect on the columnar channeling effect. Also, we are assuming that the column is continuous and straight through the entire sample thickness. Strain fields and stacking faults may induce Bloch state transitions that complicate the intuitive interpretability of the image. In practice however, these limitations can be largely overcome by the use of sufficiently thin samples, and in the future by imaging along several different zone axes.

The Z-contrast image is also relatively insensitive to sample tilt, as we might expect, since the excitation of the tightly bound s states is correspondingly insensitive to small tilts away from exact axial incidence. Calculations by Loane, Kirkland, and Silcox (1988) and Kelly and Bird (1991) have shown that the electron current follows the strings for tilts of up to half a Bragg angle, and this is confirmed experimentally by the images shown in Fig 6. Note that the image fades more rapidly for tilts along [220] than for tilts along [002], the dumbbell axis, since the intensity at the atom sites due to the ls molecular orbital states reduces more rapidly for tilts along the [220] direction. This behavior can, of course, be anticipated directly from the anisotropic shape of the central maximum in the large angle channeling pattern.

As an example of the power of intuitive inversion, Figure 7 shows part of a Si_4Ge_8 ultrathin superlattice revealing a different atomic arrangement at each interface, 2 × n interfacial ordering at the top Si on Ge interface, a [111] planar structure in the central Si layer, with Ge threading right through to the next Ge layer, and cross-like structures in the lowest Si layer. Clearly this image is totally inconsistent with the conventional wisdom of strain-enhanced interdiffusion leading to the formation of a stable ordered alloy. A previously unknown growth mechanism can however explain the various ordered arrangements observed and the asymmetric interfacial abruptness (Jesson, Pennycook, and Baribeau 1991), and the lateral size of the ordered domains correlates well with the island size observed by scanning tunneling microscopy.

Unless well documented previously, such complex interfacial arrangements would almost certainly never be considered as likely trial structures for fitting to diffraction data or to phase contrast images. Direct imaging

offers new insights into the properties of materials and their atomic scale growth mechanisms.

Restoration of High-Resolution Information

The *Z*-contrast image is given by a straightforward convolution of an object function with the intensity profile of the probe (or the effective probe, see Eq. 8). Neither of these have any associated phase, and in addition the blurring function is an order of magnitude broader than the intrinsic width of the spikes in the object function. We therefore have an ideal situation for the use of image processing techniques to restore the high frequency information lost by the convolution, and we present below some initial results using the maximum entropy method.

All images have been obtained with a VG Microscopes' HB501UX operating at an accelerating voltage of 100 kV using a high resolution pole piece (C_s = 1.3 mm), which gives a resolution limit of 2.2Å under Scherzer optimum conditions for incoherent imaging and high source demagnification. This resolution is insufficient to resolve the Si dumbbell, although images of individual dumbbells are elongated along the [001] direction as expected (see Fig. 6). Images were recorded directly onto Polaroid type 52 film using single 20 scans (line speed 20 ms), and digitized subsequently.

Figure 8 shows a small region of a Si{110} image, captured as a 256 × 256 pixels, with the corresponding maximum entropy reconstruction performed with the Cambridge MemSys 5 software of Gull and Skilling (1984). Here, a simple Gaussian point spread function was assumed, rather than the true probe profile, the width being optimized to achieve the sharpest reconstruction. With no prior knowledge of the nature of the object, the program has found it necessary to place two scattering centers within each image feature in

order to account for the intensity distribution in the image. The reconstruction has rotated the dumbbells somewhat which is a result of some sample tilt as can be seen by comparing the original data to the images shown in Fig 6. However, it still gives an average separation of 1.33 Å ± 0.20 for the two columns of a dumbbell, remarkably close to the true value of 1.36 Å. Since the reconstruction is noise limited, improved detector efficiencies, should result in accuracies such as this being achievable from individual columns in the image. Note that the analysis also quantifies the relative strengths of the scattering centers, thus automatically quantifying the compositional information in the image.

Figure 9 shows the raw image and the maximum entropy reconstruction of a high-angle grain boundary in a $YBa_2Cu_3O_{7-x}$ thin film. Viewed along the c-axis, the superconductor projects as mixed columns of Y and Ba (which are seen bright in the raw image) with Cu columns in between. The Cu columns are not visible in the image, even though the distance to the adjacent Y/Ba columns is 2.72 Å, well above the 2.2Å probe size. This is because of the presence of an amorphous surface layer on the sample created during ion milling, which broadens the probe before it reaches the crystal.

The actual point spread function was therefore estimated directly from the image, by scanning along the ⟨100⟩ directions through the centers of the Y/Ba columns. This scan would pass 1.93Å away from the lighter Cu column and therefore give a good first approximation of the true point spread function. The resulting image reconstruction seen in Fig. 4b now finds it necessary to account for the higher than expected background in the vicinity of the Cu columns, and therefore introduces additional columns. The reconstruction is still limited severely by the noise in the original data however, highlighting the importance of improving the efficiency of the annular detector.

In fact, it may well be beneficial to operate the microscope at a lower source demagnification, which would degrade the image resolution, but give substantially improved image statistics, so that the maximum entropy reconstruction might then give a higher final image resolution.

Present results, though severely noise limited, are however very encouraging since they clearly demonstrate that a factor of two resolution enhancement is quite straightforward to achieve with the Z-contrast approach.

Future Directions

At the time of writing, a 300 kV STEM is undergoing initial tests. With the higher accelerating voltage the resolution limit reduces to an anticipated 1.3 Å which would resolve the Si dumbbell directly, as seen in the simulated images of a superlattice shown in Fig. 10. The smaller probe also provides compositional sensitivity for the individual columns comprising the dumbbells. Furthermore, probe broadening effects due to amorphous surface layers will also be reduced by a factor of three compared to the present 100 kV beam, and image statistics will be improved through the use of a high quantum efficiency Howie detector and digital image acquisition.

There seems no reason to suppose that a factor of two resolution enhancement could not also be achieved at 300 kV using the maximum entropy method, since the width of the object function will still be almost an order of magnitude below the theoretical minimum probe size. Indeed, given the anticipated improvements in image statistics it is possible that greater enhancement could be achieved, although at some point the second order effects in the Z-contrast image will presumably become first order again, and it is unclear at present just how far beyond a factor of two the resolution

could be enhanced before the restoration would become sensitive to sample thickness and defocus. There may also be an increased need for molecular orbital calculations to quantify the composition of closely spaced columns, since the Bloch states are only slightly more localized at the higher accelerating voltage.

However, a factor of two enhancement would be quite sufficient to allow sub-Ångstrom information to be extracted from Z-contrast images. Incoherent imaging in the STEM overcomes many of the limitations of coherent imaging and diffraction methods, the phase problem of electron diffraction and the complications of non-linear imaging. However, once the approximate structure has been determined, the extreme sensitivity of phase contrast methods will still be valuable for structure refinement. The crucial advantage of the Z-contrast approach is that it can reveal interfacial structures not previously imagined. It directly suggests the likely atomic structure and composition which can then be used as input data for further structure refinement or for theoretical calculations of total energy or interfacial properties.

Z-contrast incoherent imaging represents a fundamentally new approach to high-resolution electron microscopy, an approach that appears capable of realizing sub-Ångstrom microscopy in an extremely simple and direct manner.

Acknowledgement

This research was sponsored by the Division of Materials Sciences, U.S. Department of Energy, under contract DE-AC05-84OR21400 with Martin Marietta Energy Systems, Inc.

References

Cherns, D., Howie, A., and Jacobs, M. H., Z. *Naturforsch.* **28a** (1973) 565.

Crewe, A. V. and Salzman, D. B., *Ultramicroscopy* **9** (1982) 373.

Gull, S. F. and Skilling, J., *IEE Proc.* **131F** (1984) 646.

Hall, C. R., *Philos. Mag.* **12** (1965) 815.

Hall, C. R. and Hirsch, P. B. , *Proc. Roy. Soc.* **A286** (1965) 158.

Howie, A., *J. Microsc.* **117** (1979) 11.

Jesson, D. E. and Pennycook, S. J., in *Proc. of the XIIth International Congress for Electron Microscopy*, Vol. 1, eds. L. D. Peachey and D. B. Williams (San Francisco Press, San Francisco, California, 1990) p. 74.

Jesson, D.E., Pennycook, S. J., and Baribeau, J.-M., *Phys. Rev. Lett.* **66** (1991) 750.

Kambe, K., *Ultramicroscopy* **10** (1982) 223.

Kelly, M. and Bird, D. M. , *Proc. 49th EMSA* meeting, ed. G. W Bailey and E. L. Hall (San Francisco Press, San Francisco, California, 1991) p. 666.

Loane, R. F., Kirkland, E. J., and Silcox, J., *Acta Cryst.* **A44** (1988) 912.

Pennycook, S. J. and Howie, A. , *Philos. Mag.* **41** (1980) 809.

Pennycook, S. J. and Jesson, D. E., *Phys. Rev. Lett.* **64** (1990) 938.

Pennycook, S. J. and Jesson, D. E., *Ultramicroscopy* **37** (1991) 14.

Scherzer, O., *J. Appl Phys.* **20** (1949) 20.

Figure Captions

Fig. 1. Schematic showing how the curvature of the Ewald sphere intercepts only the tails of the zero layer coherent reflections at high angles.

Fig. 2. Schematic of (a) a monolayer raft of Si⟨110⟩, (b) the potential for high-angle scattering (drawn approximately to scale), and (c) convolution with a 2.2 Å FWHM intensity optimum imaging probe.

Fig. 3. Schematic projection of a Si_2Ge_2 superlattice along ⟨110⟩ with corresponding axial Bloch states for a 100 kV electron, showing bonding ls molecular orbital states around individual Si and Ge dumbbells (upper states) and two less localized states as described in the text (lower states).

Fig. 4. Variation in ls molecular orbital intensity $(\varepsilon^{ls}b^{ls})^2$ with alloy composition x in ⟨110⟩ $Si_{1-x}Ge_x$.

Fig. 5. Ratio of the integrated intensity at the atom sites in Ge compared to Si as a function of thickness, using the full dynamical calculation (solid line), and the ls state alone (dashed line).

Fig. 6. Large-angle channeling pattern from Si⟨110⟩ (the Howie detector intensity in selected area mode) with Z-contrast images corresponding to various crystal tilts.

Fig. 7. Z-contrast image of a Si_4Ge_8 ultrathin superlattice revealing unexpected interfacial arrangements and ordering.

Fig. 8. (a) Z-contrast image of Si⟨110⟩ and (b) maximum entropy reconstruction indicating the presence of dumbbells.

Fig. 9. (a) Image of a high-angle grain boundary in $YBa_2Cu_3O_{7-x}$ and (b) maximum entropy reconstruction revealing Cu columns not visible in the original data.

Fig. 10. Simulated images of interfacial ordering in a Si_4Ge_8 superlattice at (a) 100 kV and (b) 300 kV accelerating voltages.

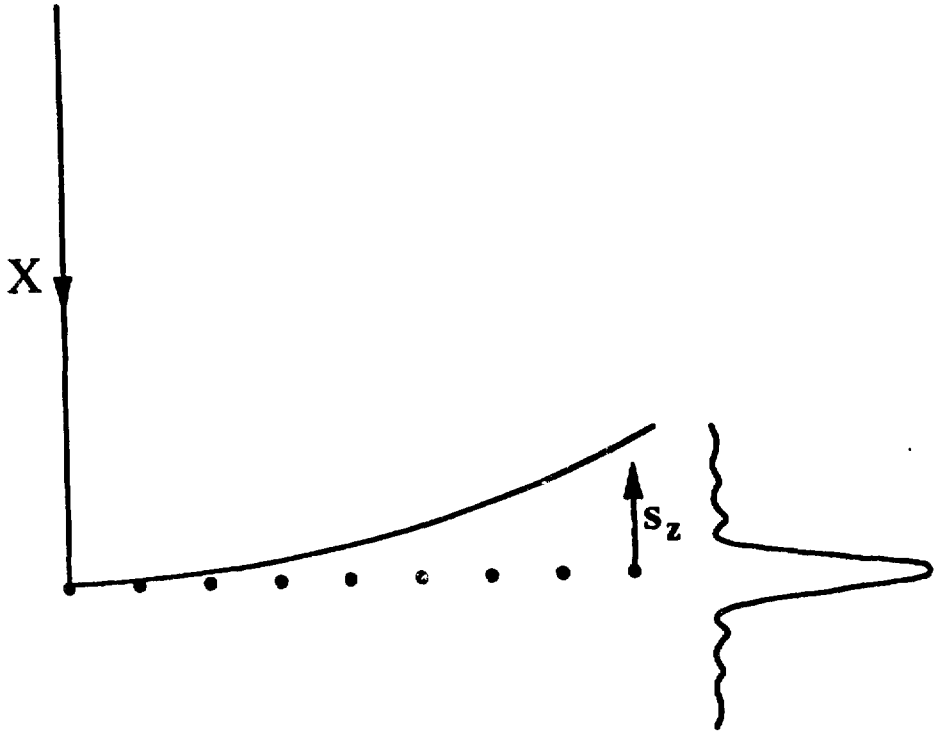
X
S_z

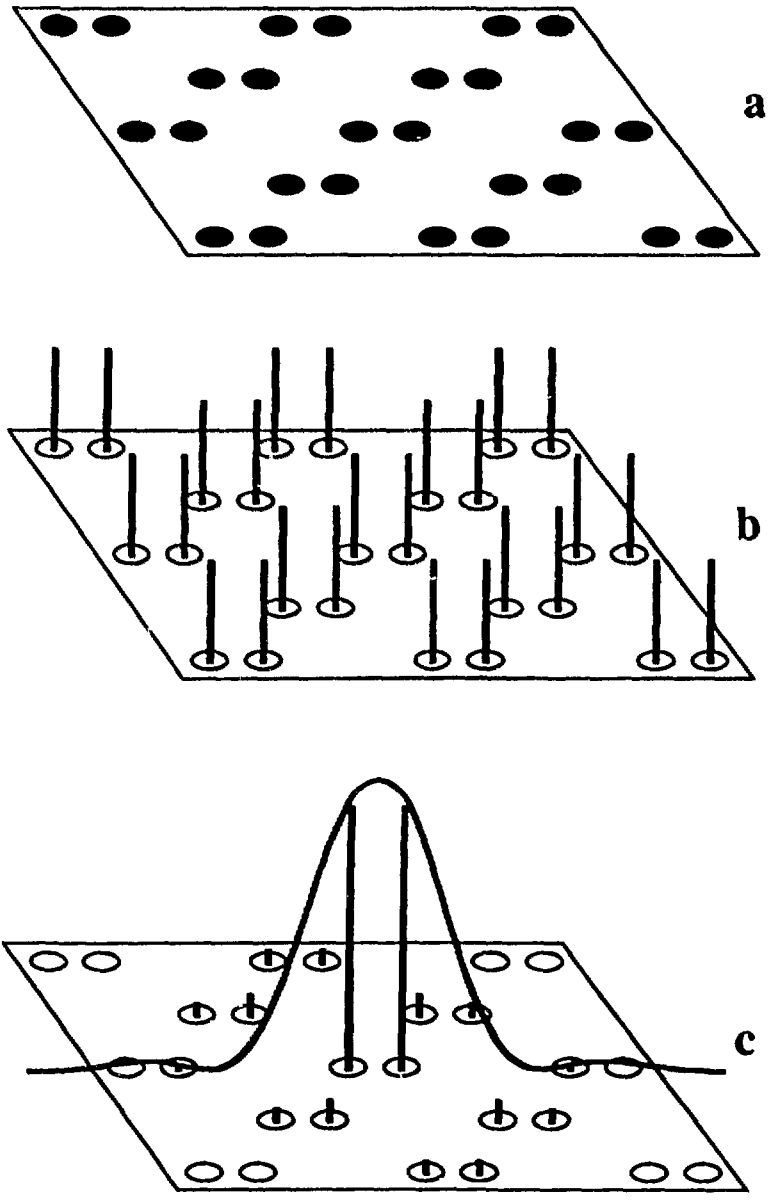
a
b
c

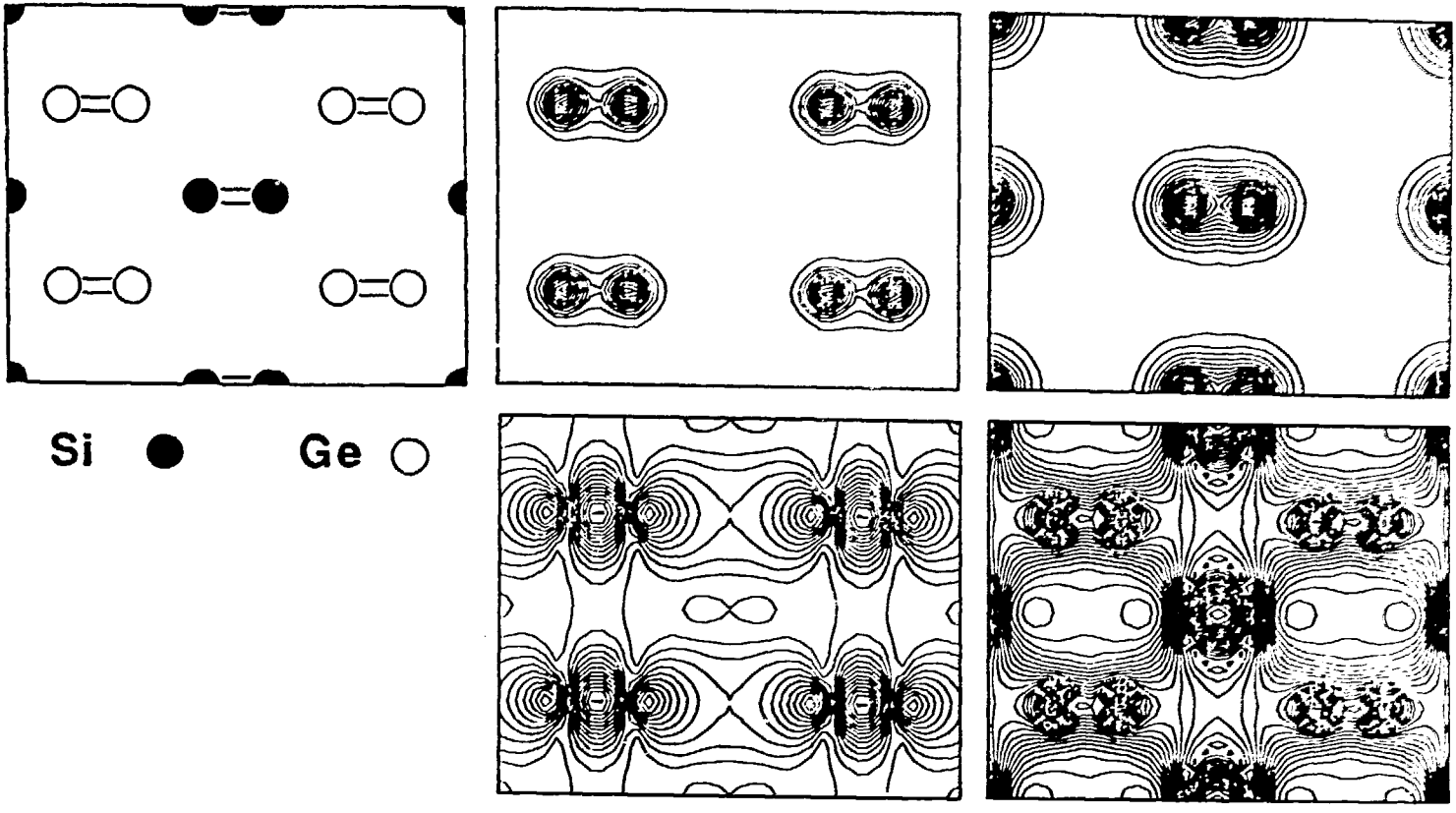
Si
Ge

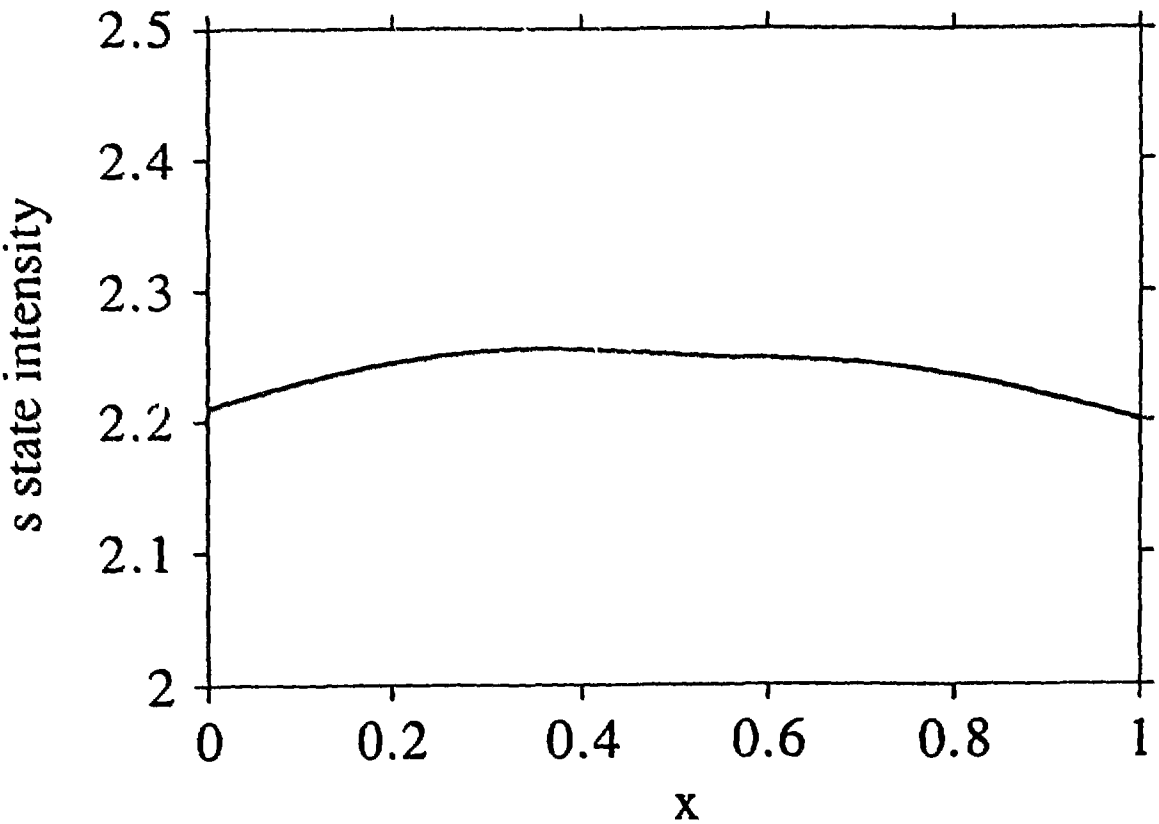
2.5
2.4
2.3
2.2
2.1
2
s state intensity
0
0.2
0.4
0.6
0.8
1
x

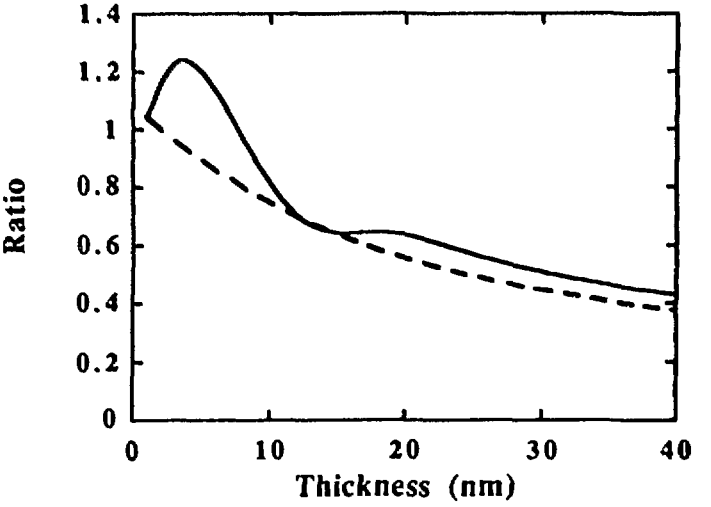
1.4
1.2
1
0.8
0.6
0.4
0.2
0
Ratio
0
10
20
30
40
Thickness (nm)

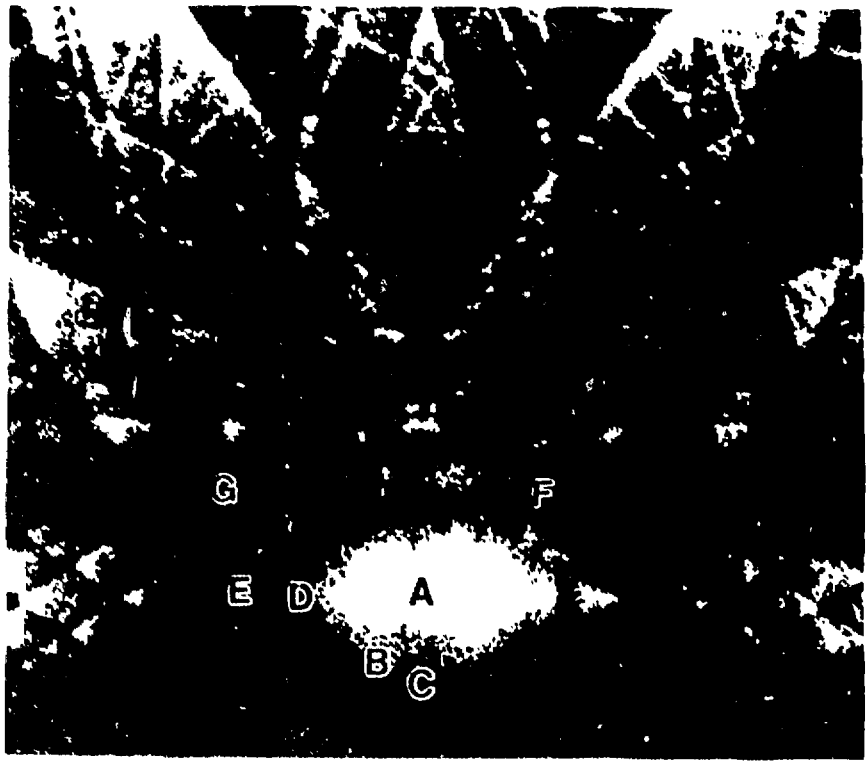


A

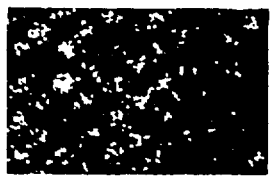
B


C

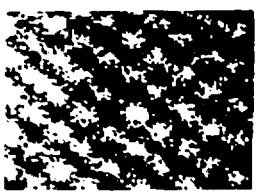
D


E

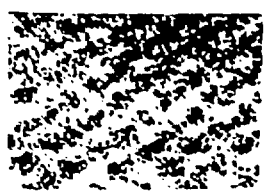
F

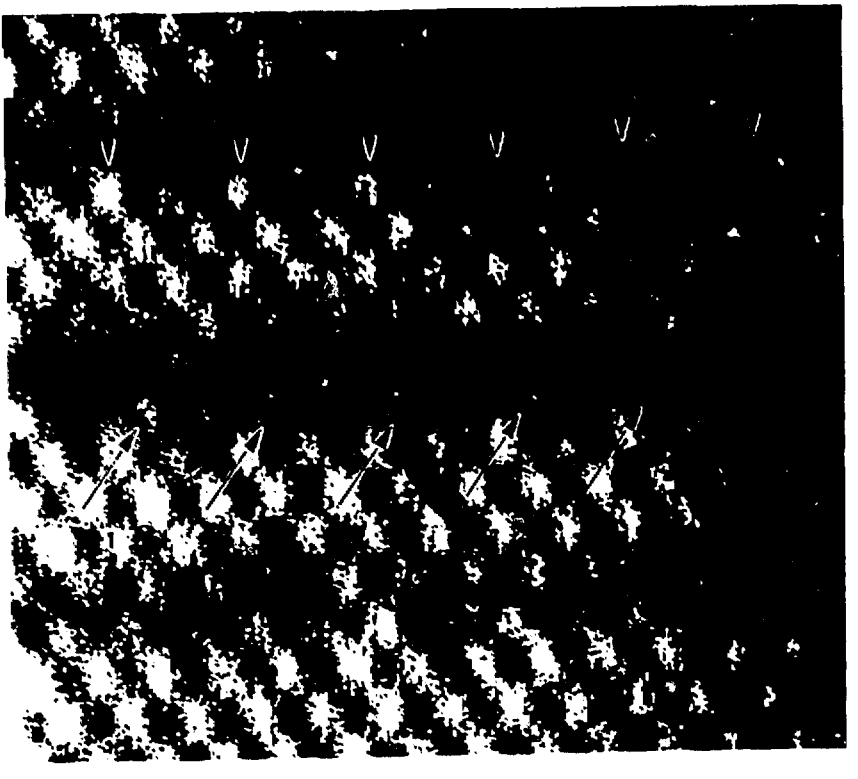

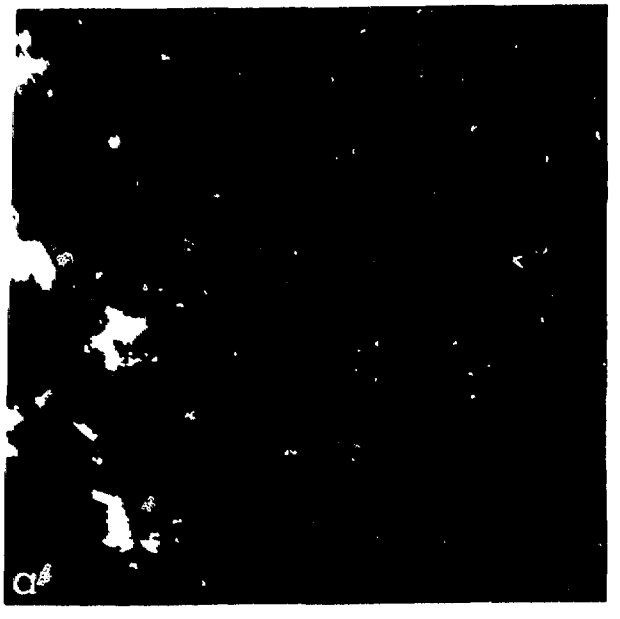
a

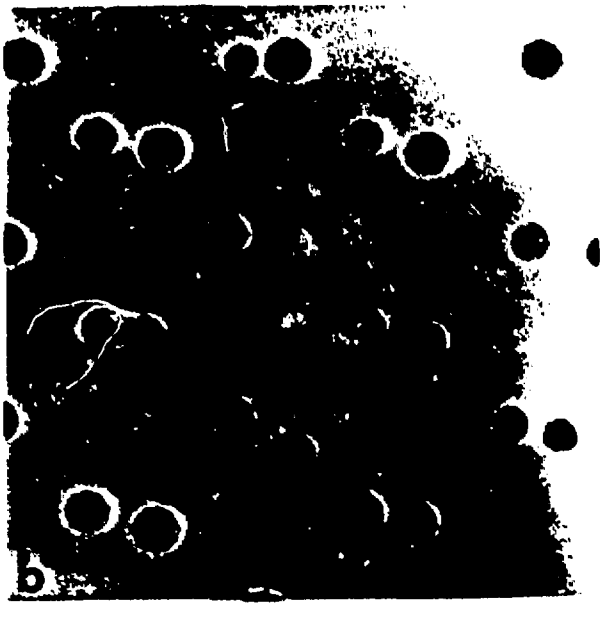
b

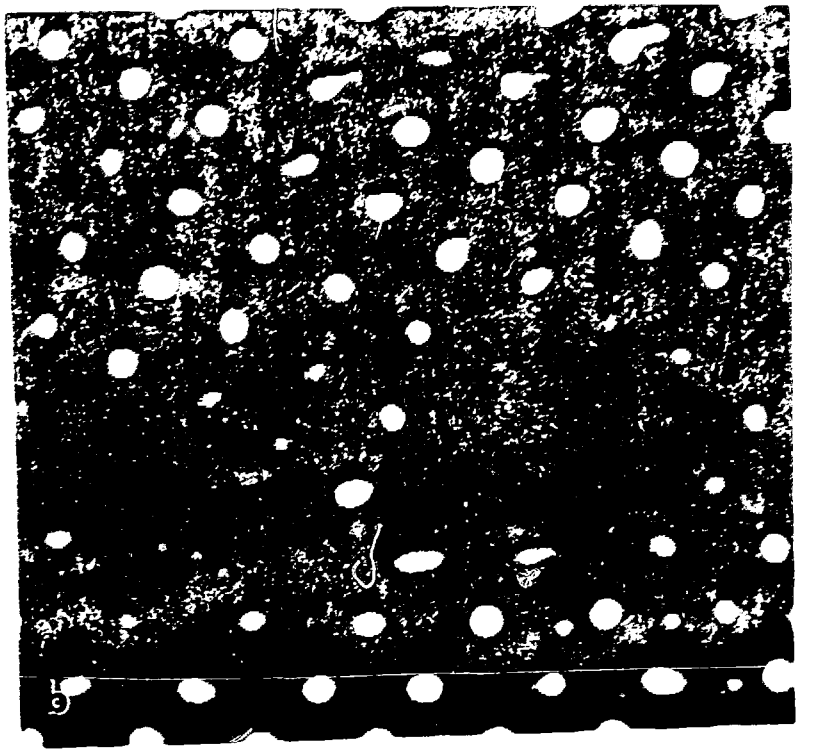

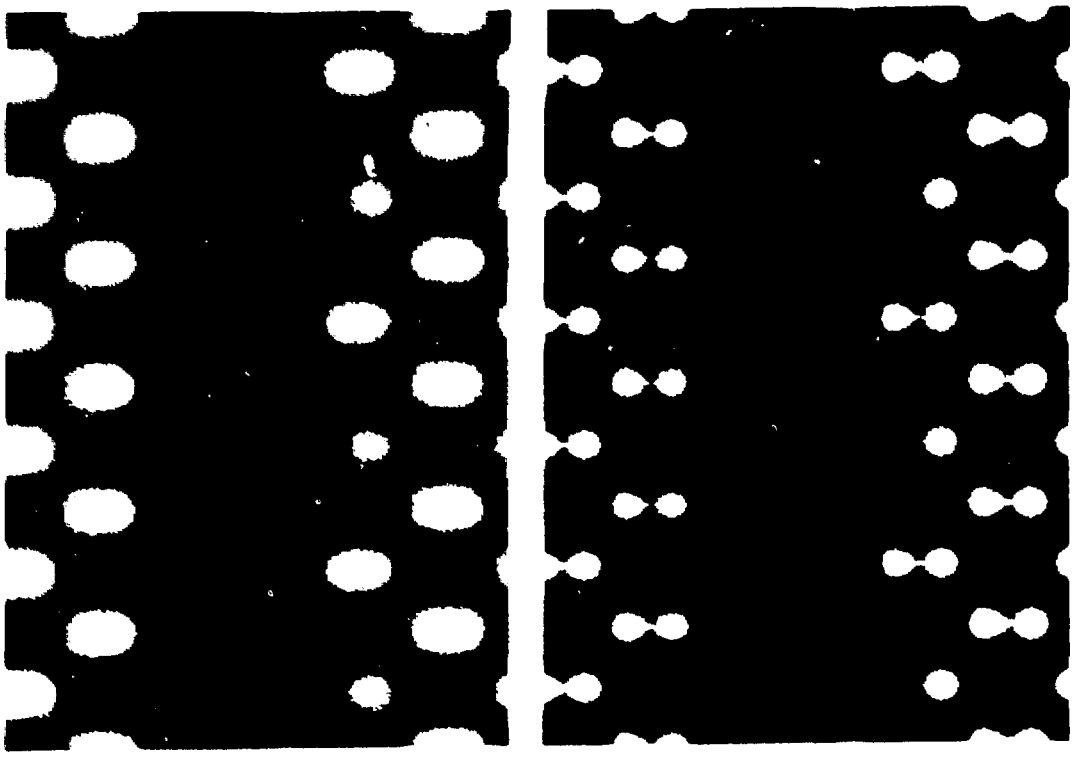

a b